

Deep Shape-from-Template: Wide-Baseline, Dense and Fast Registration and Deformable Reconstruction from a Single Image

David Fuentes-Jimenez, David Casillas-Perez, Daniel Pizarro
Universidad de Alcalá

{d.fuentes, david.casillas}@edu.uah.es, daniel.pizarro@uah.com

Toby Collins

Institut de Recherche contre les Cancers de l'Appareil Digestif

toby.collins@gmail.com

Adrien Bartoli

Université Clermont-Auvergne

adrien.bartoli@gmail.com

April 8, 2022

Abstract

We present Deep Shape-from-Template (DeepSfT), a novel Deep Neural Network (DNN) method for solving real-time automatic registration and 3D reconstruction of a deformable object viewed in a single monocular image. DeepSfT advances the state-of-the-art in various aspects. Compared to existing DNN SfT methods, it is the first fully convolutional real-time approach that handles an arbitrary object geometry, topology and surface representation. It also does not require ground truth registration with real data and scales well to very complex object models with large numbers of elements. Compared to previous non-DNN SfT methods, it does not involve numerical optimization at run-time, and is a dense, wide-baseline solution that does not demand, and does not suffer from, feature-based matching. It is able to process a single image with significant deformation and viewpoint changes, and handles well the core challenges of occlusions, weak texture and blur. DeepSfT is based on residual encoder-decoder structures and refining blocks. It is trained end-to-end with a novel combination of supervised learning from simulated renderings of the ob-

ject model and semi-supervised automatic fine-tuning using real data captured with a standard RGB-D camera. The cameras used for fine-tuning and run-time can be different, making DeepSfT practical for real-world use. We show that DeepSfT significantly outperforms state-of-the-art wide-baseline approaches for non-trivial templates, with quantitative and qualitative evaluation.

1 Introduction

The joint task of registration and 3D reconstruction of deformable objects from RGB videos and images is a major objective in computer vision, with numerous potential applications, for instance in augmented reality. In comparison with other mature 3D reconstruction problems, such as Structure-from-Motion (SfM) where rigidity is imposed on the scene [25], deformable registration and 3D reconstruction present significant unsolved problems. Two main scenarios exist in this task: Non-Rigid SfM (NRSfM) [8, 27, 47, 11] and Shape-from-Template (SfT) [42, 6, 35, 10]. NRSfM reconstructs the 3D shape of a deformable object from multiple RGB images. In contrast, SfT reconstructs the 3D shape from a single RGB

image using an object *template*. The template includes knowledge about the object’s appearance, shape and permissible deformations. These are typically represented by a texture-map, a 3D mesh and a simple mechanical model. SFT is suitable for many applications where the template is known or can be acquired, using for instance SfM or any available 3D scanning solution.

SFT solves two fundamental and intimately related problems: *i*) template-image *registration*, which associates pixels in the image to their corresponding locations in the template, and *ii*) *shape inference*, which recovers the observed 3D shape or equivalently the template’s 3D deformation. The majority of SFT methods focus on solving shape inference assuming that registration is independently obtained with existing feature-based or dense methods [39, 19, 14]. In all other cases, both problems are solved simultaneously using tracking with iterative optimization [35, 13, 3]. To date there exists no non-DNN wide-baseline SFT method capable of solving both problems densely and in real-time. DNN SFT methods have been very recently proposed [40, 20], following the success of the DNN methodology in related problems such as 3D human pose estimation [33, 22], depth [16, 18, 28] and surface normal reconstruction with rigid objects [5, 45]. The general idea is to learn the function that maps an input image to the template’s 3D deformation parameters from training data. This has the potential to jointly solve registration and shape inference and eliminates the need for iterative optimization at run-time. These two recent methods are promising but bear important limitations. First, they are limited to flat templates described by regular meshes with very small vertex counts. Second, they require ground-truth registration for training, which is practically impossible to obtain for real data.

We propose DeepSFT, the first DNN SFT method based on a fully-convolutional network without the above limitations. DeepSFT has the following desirable characteristics. 1) It is dense and provides registration and 3D reconstruction at the pixel level. 2) It does not require temporal continuity and handles large deformations and pose changes between the template and the object. 3) It runs in real-time using conventional GPU hardware. 4) It is applicable for templates with arbitrary geometry, topology and surface representation, including meshes, implicit and explicit functions such as NURBS. 5) It is highly robust and handles well the major challenges of SFT, including self

and external occlusions, illumination changes and blur. 6) Training involves a novel combination of supervised learning with synthetic data and semi-supervised learning with RGB-D real data. Crucially, we do not require ground-truth registration for the real training data but only RGB-D. Compared to previous approaches, this makes it feasible to acquire the real training data *automatically*, and therefore feasible to deploy it in real settings. 7) The network complexity, training cost and running cost are independent of the template representation, for instance of the mesh vertex count. It therefore scales very well to highly complex templates with detailed geometry that were, until now, not solvable in real-time. There exists no previous method in the literature with the above characteristics. Our method thus pushes SFT significantly forward. We present quantitative and qualitative experimental results showing that our method concretely outperforms in accuracy, robustness and computation time.

2 Previous Work

We first review the non-DNN SFT methods, forming the vast majority of existing work. We start with the shape inference methods and then the integrated methods combining shape inference and registration. We finally review the recent DNN SFT methods.

Shape inference methods. The shape inference methods assume that the registration between the template and the image is given, which is a fundamental limiting factor of applicability. We classify them according to the deformation model. The most popular deformation model is isometry, which attempts to approximately preserve the geodesic distance, and has been shown to be widely applicable. *Isometric* methods follow three main strategies: *i*) Using a convex relaxation of isometry called inextensibility [41, 42, 37, 9], *ii*) using local differential geometry [6, 10] and *iii*) minimizing a global non-convex cost [9, 36]. Methods in *iii*) are the most accurate but also the most expensive. They require an initial solution found using a method from *i*) or *ii*). There also exist *non-isometric* methods, with the angle preserving conformal model [6] or simple mechanical models with linear [32, 31] and non-linear elasticity [23, 24, 2]. These models all require boundary conditions in the form of

known 3D points, which is another fundamental limiting factor of applicability. Their well-posedness remain open research questions.

Integrated methods. The integrated methods compute both registration and shape inference. We classify them according to their ability to handle wide-baseline cases. *Short-baseline* methods are restricted to video data and may work in real time [35, 13, 29]. They are based on the iterative minimization of a non-convex cost and use keypoint correspondences [35] or optic flow [13, 29]. The latter supports dense solutions and resolve complex, high-frequency deformations. Their main limitations are two-fold. First, they break down when there is fast deformation or camera motion. Second, at run-time, they must solve an optimization process that is highly computationally demanding, requiring careful hand-crafted design and balancing of data and deformation constraints. In contrast, *wide-baseline* SfT methods can deal with individual images showing the object with strong deformation without priors on the camera viewpoint [35, 12]. These methods solve registration sparsely using keypoints such as SIFT [30] with filtering to reduce the mismatches [39, 38]. The main limitations of these methods are two-fold. First, they are fundamentally limited by the feature-based registration, which fails due to a weak or repetitive texture, low image resolution, blur or viewpoint distortion. second, they require to solve a highly demanding optimization problem at run-time. Because of these limitations, the existing wide-baseline methods have only been shown to work for simple objects with simple deformations, such as bending sheets of paper.

DNN SfT methods. Two DNN SfT methods [40, 20] have been recently proposed. They address isometric SfT by learning the mapping between the input image and the 3D vertex coordinates of a regular mesh. Both methods use regression with a fully-convolutional encoder. They require the template to be flat and to contain a smaller number of regular elements. In [40] belief maps are obtained for the 2D position of the vertices which are then combined with depth estimation and reprojection constraints to recover their 3D positions. This considerably limits the size of the mesh, as shown by the reported examples with fewer than 10×10 vertex counts. Both meth-

ods were trained and tested with synthetically generated images. Only [40] provides results on a real video of a bending paper sheet, but required ground-truth registration and shape to fine-tune the network on part of the video. These two methods thus form a preliminary step toward applying DNN to SfT, but are strongly limited by the low template complexity and requirement for ground truth registration. Indeed, even if depth may be relatively easy to obtain for training, ground truth registration is extremely difficult to measure for real data.

3 Problem Formulation

Figure 1 shows the geometrical model of SfT. The *tem-*

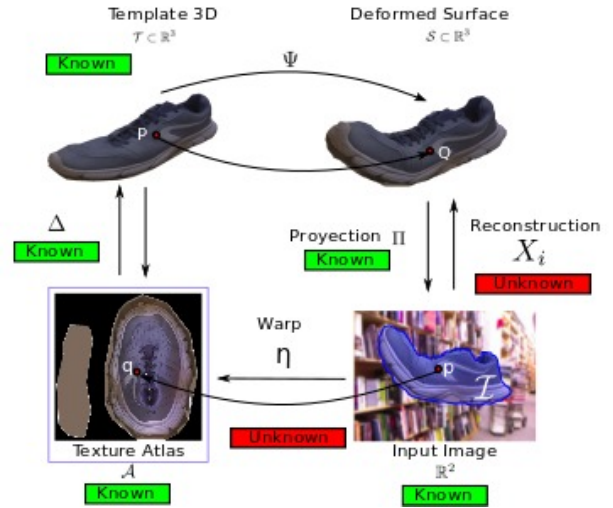


Figure 1: Differential Geometrical Model

plate is known and represented by a 3D surface $\mathcal{T} \subset \mathbb{R}^3$ jointly with its appearance, described as a *texture map* \mathcal{A} . The texture map is standard and represented as a collection of flattened *texture charts* \mathcal{U}_i whose union cover the appearance of the whole *template*, as seen in Figure 1. In our approach *templates* are not restricted to a specific topology, modelling both *thin-shell* and *volumetric* objects. They are also not restricted by a specific representation. In our experimental section we use mesh representations because of their generality, but this is not a requirement of the method. The bijective map between \mathcal{A}

and \mathcal{T} is known and denoted by $\Delta : \mathcal{A} \mapsto \mathcal{T}$. We assume that the *template* surface \mathcal{T} is deformed with an unknown *quasi-isometric* map $\Psi : \mathcal{T} \mapsto \mathcal{S}$, where $\mathcal{S} \subset \mathbb{R}^3$ denotes the unknown deformed surface. *Quasi-isometric* maps permit localized extension/compression, common with real world deforming objects.

The input image is modeled as the colour intensity function $I : \mathbb{R}^2 \mapsto (r, g, b)$, which is discretized into a regular grid of pixels in the retinal plane. The visible part $\mathcal{S}_v \subset \mathcal{S}$ of the surface is projected on an unknown subset of the image plane $\mathcal{I} \subset \mathbb{R}^2$. We assume the perspective camera for projection:

$$\begin{aligned} \Pi_p : \quad \mathbb{R}^3 &\mapsto \mathbb{R}^2 \\ (x, y, z) &\mapsto \left(\frac{x}{z}, \frac{y}{z} \right), \end{aligned} \quad (1)$$

where \mathcal{S}_v is represented with a perspective embedding $X_v : \mathcal{I} \mapsto \mathcal{S}_v$ with $X_v(u, v) = \rho(u, v)(u, v, 1)$.

We assume X_v is known and any lens distortion is either negligible or has been corrected. The depth function $\rho : \mathcal{I} \mapsto \mathcal{S}_v$ represents the depth coordinate of \mathcal{S}_v from the camera's coordinate system. In the absence of self-occlusions, $\mathcal{S}_v = \mathcal{S}$. Volumetric *templates* always induce self-occlusions in the image.

The unknown registration function, or *warp*, $\eta : \mathcal{I} \mapsto \mathcal{A}$ is an injective map that relates each point of \mathcal{I} to its corresponding point in \mathcal{A} .

4 Network architecture

We propose a DNN, hereinafter *DeepSfT*, that estimates $\rho(u, v)$ and $\eta(u, v)$ directly from the input image $I(u, v)$:

$$(\hat{\rho}, \hat{\eta}) = \mathcal{D}(I, \theta_{\mathcal{T}}), \quad (2)$$

where $\hat{\rho}$ and $\hat{\eta}$ are normalized ($\hat{\rho} \in [-1, 1]$, $\hat{\eta} \in [-1, 1] \times [-1, 1]$) and discretized versions of ρ and η . Our method also recovers \mathcal{I} as both ρ and η are equal to -1 outside the domain \mathcal{I} of the image. In this sense *DeepSfT* performs object segmentation at a pixel level. $\theta_{\mathcal{T}}$ are the network weights, that depend on the *template* \mathcal{T} , and are learned with training (see Section 6). *DeepSfT* has been trained to recognize a specific *template* so a large amount of deformations are required as described in Section 5.

Figure 2 shows the proposed network architecture. The complete architecture receives an RGB input image I_i

with a resolution of $h_i \times w_i = 270 \times 480$ pixels and returns the estimated depth map $\hat{\rho}_i$ and the registration maps $\hat{\eta}_i$. Both $\hat{\eta}_i$ and $\hat{\rho}_i$ have the same size as the input image.

DeepSfT is divided into two main blocks: the *main block* is modelled on an *encoder-decoder* architecture, very similar to those used in semantic segmentation [4]. This gives a first depth map estimation and the proposed registration function $\hat{\eta}_i$. The second one is a *domain adaptation block* that uses the RGB input image I_i together with the output of the previous block to refine the depth map estimation $\hat{\rho}_i$. This cascade topology where the input image is feed into refinement blocks has proven to improve the results obtained using single stages in methods for 3D depth estimation [17]. This block is also crucial to adapt the network to real data as described in Section 6.

Both the *main* and *domain adaptation blocks* use identity, convolutional and deconvolutional residual feed-forwarding structures based on the ResNet50 [43] (see Figure 3). Each block is composed of two unbalanced parallel branches with convolutional layers that propagate the information forward into deeper layers, preserving the high frequencies of the data.

Table 1 shows the layered decomposition of the *main block*. It first receives the RGB input image and performs a first reduction of the input size. Then, a sequence of three *convolutional and identity blocks* encode texture and the depth information as deep features. Information is reduced to a compressed feature vector in a representation space of dimension $12 \times 20 \times 1024$. Information related with the deformable surface is coded in this vector per each RGB input image.

Decoding is performed with *decoding blocks*. These require upsampling layers to increase the dimensions of the input tensors before passing through the convolution layers, as shown in Figure 3.c. Finally, the last layers consist of CNNs and cropping layers that adapt the output of the decoding block to the size of the output maps ($270 \times 480 \times 3$). The first channel provides the depth estimate and the last two channels provide the registration warp.

Table 2 shows the layered decomposition of the *domain adaptation block*. It is a reduced version of the *main block* where only the first two *encoding and decoding blocks* are included. The *domain adaptation block* take as input the concatenation of the input image and the output from the

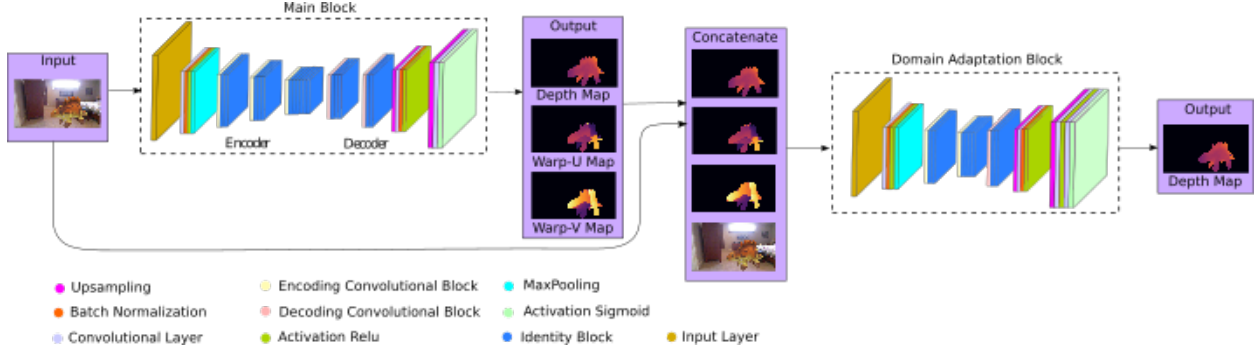


Figure 2: DeepSfT architecture. The proposed network architecture is composed of two principal blocks, the *main block* and the *domain adaptation block*. Each block is an *encoder-decoder* scheme tailored for SfT. The *Main block* receives an RGB input image, process it and gives a first depth map estimate along with the warp. The *domain change block* collects the depth and warp estimation from the *main block* and the RGB input image to create a final refined depth map

Layer num	Type	Output size	Kernels/Activation
1	Input	(270,480,3)	—
2	Convolution 2D	(135,240,64)	(7,7)
3	Batch Normalization	(135,240,64)	—
4	Activation	(135,240,64)	Relu
5	MaxPooling 2D	(45,80,64)	(3,3)
6	Encoding Convolutional Block	(45,80,[64, 64, 256])	(3,3)
7-8	Encoding identity Block x 2	(45,80,[64, 64, 256])	(3,3)
9	Encoding Convolutional Block	(23,40,[128, 128, 512])	(3,3)
10-12	Encoding identity Block x 3	(23,40,[128, 128, 512])	(3,3)
13	Encoding Convolutional Block	(12,20,[256, 256, 1024])	(3,3)
14-16	Encoding identity Block x 3	(12,20,[256, 256, 1024])	(3,3)
17-20	Encoding identity Block x 3	(12,20,[1024, 1024, 256])	(3,3)
21	Decoding Convolutional Block	(24,40,[512, 512, 128])	(3,3)
22	Cropping 2D	(23,39,128)	(1,1)
23-25	Encoding identity Block x 3	(23,39,[512, 512, 128])	(3,3)
26	Decoding Convolutional Block	(46,78,[256, 256, 64])	(3,3)
27	Zero Padding	(46,80,64)	(0,1)
28-29	Encoding identity Block x 2	(46,80,[256, 256, 64])	(3,3)
30	Upsampling	(138,240,64)	(3,3)
31	Cropping 2D	(136,240,64)	(2,0)
32	Convolution 2D	(136,240,64)	(7,7)
33	Batch Normalization	(135,240,64)	—
34	Activation	(136,240,64)	Relu
35	Upsampling	(272,480,64)	(3,3)
36	Cropping 2D	(270,480,64)	(2,0)
37	Convolution 2D	(272,480,3)	(3,3)
38	Activation	(270,480,1)	Linear

Table 1: Main block architecture.

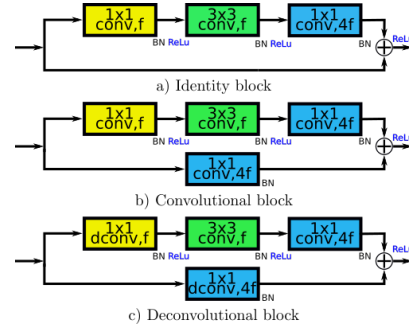


Figure 3: Identity, convolutional and deconvolutional residual blocks.

main block (6 channels) and it outputs a new refined depth map.

5 Training

We create a quasi-photorealistic SfT synthetic database using simulation software. Synthetic data allows us to easily train our DNN end-to-end. We then follow by re-training the *domain adaption* block using a much smaller dataset collected using a standard RGB-D sensor. We recall that there are no public training datasets of this kind.

Layer num	Type	Output size	Kernels/Activation
1	Input	(270,480,3)	–
2	Convolution 2D	(135,240,64)	(7,7)
3	Batch Normalization	(135,240,64)	–
4	Activation	(135,240,64)	Relu
5	MaxPooling 2D	(45,80,64)	(3,3)
6	Encoding Convolutional Block	(45,80,[64, 64, 256])	(3,3)
7-8	Encoding identity Block x 2	(45,80,[64, 64, 256])	(3,3)
9	Encoding Convolutional Block	(23,40,[128, 128, 512])	(3,3)
10-13	Encoding identity Block x 4	(23,40,[128, 128, 512])	(3,3)
14	Decoding Convolutional Block	(46,80,[512, 512, 128])	(3,3)
15-16	Encoding identity Block x 2	(46,80,[512, 512, 128])	(3,3)
17	Upsampling	(92,160,128)	(2,2)
18	Cropping 2D	(92,160,128)	(2,0)
19	Convolution 2D	(90,160,64)	(3,3)
20	Batch Normalization	(90,160,64)	–
21	Activation	(90,160,64)	Relu
22	Upsampling	(270, 480, 64)	(3,3)
23	Convolution 2D	(270, 480, 32)	(3,3)
24	Activation	(270, 480, 32)	Relu
25	Convolution 2D	(272,480,1)	(3,3)
26	Activation	(270,480,1)	Linear

Table 2: Domain adaptation block architecture. The block achieves to adapt the network to real data domain

5.1 Synthetic Data

This process involves randomized sampling from the object’s deformation space, generating the resulting deformation, and rendering from randomized viewpoints. We now describe the process for generating these training datasets for the templates used in the experiential section below (two thin-shell and two volumetric templates, see Table 3). *DB1* corresponds to a *DIN A4* piece of poorly-texture paper. *DB2* has the same shape as *DB1* but with a richer texture. *DB3* is a soft child’s toy and *DB4* is an adult sneaker. We emphasize that no previous work has been able to solve SfT for these last two objects in wide-baseline. The rest shape surfaces for *DB3* and *DB4* are obtained with triangulated meshes built using SfM (Agisoft Photoscan [1]).

We use *Blender* [7] to sample the deformation spaces and to create quasi-photorealistic renderings. It includes a physics simulation engine to simulate deformations with different degrees of stiffness using position based dynamics. For the paper templates we used Blender’s cloth simulator using a high stiffness term to model the stiffness of paper, with contour conditions and tensile and compressive forces in randomized 3D directions. This generates continuous deformation videos. For the other two templates we used rig-based deformation with hand-crafted rigs. This generates non-continuous deformation instances, using randomized joint angle configurations.

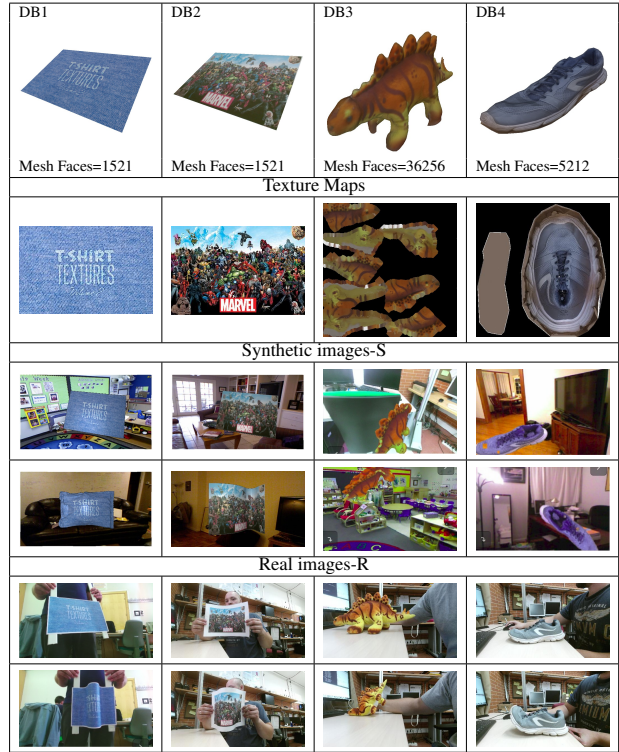


Table 3: First row shows four *templates* of the databases *DB1*, *DB2*, *DB3* and *DB4*. Next three rows show different synthetic deformation images of the *templates*. The last three rows represent real deformations of the *templates*.

For each deformation we generate random viewpoint variations with random rotations and translations of the camera, lighting variations using different specular light models and random backgrounds obtained with [34]. In total, each dataset consists of 60.000 RGB images, depth maps, and registrations (2-channel optical flow maps between the image and the template’s texturemap). All images have a resolution of 480×270 to fit the input/output of the network. We refer the reader to the supplementary material for a copy of these datasets with rigs and simulation parameters.

5.2 Real Data

We used *Microsoft Kinect v2* to record a total of 5.000 RGB-D frames of the four objects while undergoing de-

formations induced by hand manipulation, and viewpoint changes (see Table 3). Image resolution was downsized to 480×270 to fit the input shape of the network.

6 Training Procedure

The training procedure is divided in two main steps: 1) training with synthetic data followed by 2) semi-supervised fine-tuning with real data. In step 1) both *main* and *domain adaptation blocks* are trained end-to-end as a single block. We use ADAM [15] optimization with 10^{-3} learning rate and parameters $\beta_1 = \beta_2 = 0.9$. We train for 40 epochs with a batch size of $bs = 7$. We initialize *DeepSfT* with uniform random weights [46]. The loss function is defined as follows:

$$\begin{aligned} \mathcal{L}_s(I_i, \rho_i, \eta_i, \theta_{\mathcal{T}}) &= \mathcal{L}_1(I_i, \eta_i, \theta_{\mathcal{T}}) + \mathcal{L}_2(I_i, \rho_i, \theta_{\mathcal{T}}) = \\ &= \frac{1}{N_1} \sum_{i=1}^{N_1} \|\hat{\eta}_i - \eta_i\|^2 + \frac{1}{N_2} \sum_{i=1}^{N_2} \|\hat{\rho}_i - \rho_i\|^2 \end{aligned} \quad (3)$$

where $\hat{\rho}_i$ and $\hat{\eta}_i$ are the output depth map and warp estimates given by *DeepSfT* respectively. The terms ρ_i and η_i are the respective ground truths, and $N_1 = 2h_i w_i bs$ and $N_2 = h_i w_i bs$ are constants. The symbol $\|\cdot\|$ denotes the Euclidean norm. Observe that $\hat{\rho}$ and $\hat{\eta}$ inherently depend on the network weights $\theta_{\mathcal{T}}$ and on the input image I_i , see Eq. (2). In step 2) we train the *domain adaptation block* using real data while freezing the weights of the *main block*. This step is crucial to adapt the network to handle the ‘render gap’ and include the appearance characteristics of real data, such as the complex illumination, camera response and color balance. Also crucial is the fact that this can be done automatically, without the need for ground truth registration. We use stochastic gradient descend (SGD) with a small and fixed learning rate of 10^{-5} . We train the network during 10 epochs with a batch size of $bs = 7$. Having both a low learning rate and a reduced number of epochs allows us to adapt our network to real data while avoiding overfitting. In this step a different loss function \mathcal{L}_r is used, which only includes the depth information given by the depth sensor as the target

of the *domain adaptation block*:

$$\mathcal{L}_r(I_i, \rho_i, \theta_{\mathcal{T}}) = \mathcal{L}_2(I_i, \rho_i, \theta_{\mathcal{T}}) = \frac{1}{N_2} \sum_{i=1}^{N_2} \|\hat{\rho}_i - \rho_i\|^2, \quad (4)$$

where $N_2 = h_i w_i bs$.

7 Experimental Results

We evaluate *DeepSfT* in terms of 3D reconstruction and registration error with synthetic and real test data (described in §5.2). Synthetic test data was generated using the same process as the synthetic training data, using new randomized configurations not present in the training data. Real test data was generated using the same process as the real training data, using new video sequences, consisting of new viewpoints and object manipulations not present in the training data. We also generated new test data using two new cameras, as described below in §7.3.

We compare *DeepSfT* against a state-of-the-art isometric SfT method [10] refereed as *CH17*. We provide this method with two types of registration: *CH17+GTR* uses the ground truth registration (indicating its best possible performance independent of the registration method) and *CH17+DOF* using the output of a state-of-the-art dense optical flow method [44]. In the latter case we generate registration for image sequences using frame-to-frame tracking. We also compare these two variants using a *posteriori* deformation refinement using Levenberg-Marquardt, which is standard practice for improving the output of closed-form SfT methods. We refer to these improvements as *CH17R+GTR* and *CH17R+DOF*. We compare *DeepSfT* with two DNN-based methods: The first is a naïve application of the popular Resnet architecture [43] to SfT, referred as *R50F*. We performed this by removing the final two layers of Resnet and introducing one dense layer with 200 neurons and a final dense layer with a 3-channel output (for depth and warp maps) of the same size as the input image. We trained *R50F* with exactly the same training data as *DeepSfT* and real-data fine tuning. Fine-tuning was implemented by optimizing the depth loss while forcing the warp outputs to be unchanged, using the same optimizer and learning rate as we used for *DeepSfT*. The second DNN method is [20], applicable only for DB1 and DB2. Because public code

is not available, we carefully re-implemented it, requiring an adaption of the image input size and the mesh size, so that it matched the size of meshes for DB1 and DB2. We refer to this as *HDM-net*.

We evaluate reconstruction error using the root mean square error (RMSE) between the 3D reconstruction and the ground truth in millimeters. We also use RMSE to evaluate the registration accuracy in pixels. The evaluation of registration accuracy is notoriously difficult for real data, because there is no way to reliably obtain ground truth. We propose to use as a proxy for the ground truth the output from a state-of-the-art dense trajectory optical flow method *DOF*. We only make this evaluation for video sequence data, for which *DOF* can reliably estimate optical flow over the sequence.

7.1 Experiments with thin-shell objects and continuous test sequences

We show in Tables 4 and 6 the quantitative and qualitative results obtained with the thin-shell templates *DB1* and *DB2* with synthetic test datasets, denoted by *DB1S* and *DB2S*, and real test datasets, denoted by *DB1R* and *DB2R*. In terms of reconstruction error *DeepSfT* is considerably better than other methods, both in synthetic data, where the error remains below 2mm, and for real data, where the error is below 10mm. The Kinect V2 have an uncertainty of about 10mm at a distance of one meter, which partially explains the higher error for real data. The second and third best methods are *R50F* and *HDM-net*, also based on deep learning. However their results are far from those of *DeepSfT*. The method *CH17* obtains reasonable results when it is provided with ground truth registration (*CH17-GTR* and *CH17R-GTR*). However, the performance is considerably worse when real registration is provided using dense optical flow (*CH17-DOF* and *CH17R-DOF*).

In terms of registration error, *DeepSfT* also has the best results both for synthetic test data, where ground-truth registration is available, and in real test data, where *DOF* is used as the proxy. In all cases *DeepSfT* has a mean registration error approximately 2 pixels. The performance of *R50F* is competitive with *DOF*, with registration errors approximately 5 pixels. We note that *DOF* exploits temporal coherence while *RF50* and *DeepSfT* do not and

process each frame independently.

7.2 Experiments with volumetric objects and non-continuous test images

The quantitative and qualitative results of the experiments for volumetric templates *DB3* and *DB4* are provided in Tables 5 and 6 with both synthetic test data, denoted by *DB3S* and *DB4S*, and real test data, denoted by *DB4R* and *DB4R*. In this case we only provide registration error with synthetic data, because reliable registration using *DOF* is impossible with non-continuous test images. The method *CH17+GTR* and *CH17R+GTR* is tested only in the case of *DB4S*, because this is the only case that it can work (requiring a continuous texture map and a registration).

We observe a similar trend as with the thin-shell objects. *DeepSfT* is the best method both in terms of 3D reconstruction, with errors of the order of millimeters, and in registration with errors close to 2 pixels. The second best method is *R50F* although its results are significantly worse than those obtained by *DeepSfT*. The results of *CH17* and its variants are very poor. This may be due to the fact that *CH17* is not a method well adapted for volumetric objects with non-negligible deformation strain.

We show in Table 7 qualitative reconstruction results obtained with *DB1*, *DB3* and *DB4* with real images. We observe that shapes recovered with *DeepSfT* are similar to ground-truth obtained with the RGB-D camera. We can observe that the error is larger near self-occlusion boundaries. Errors for *DB1* are qualitatively smaller than for volumetric objects, which is consistent with Tables 4 and 5.

7.3 Experiments with other cameras

We now present experiments showing the ability of *DeepSfT* to be used with a different camera at run-time, without any fine tuning with the new camera. The different cameras are an Intel Realsense D435[26] (an RGB-D camera that we use for quantitative evaluation) and a Go-pro Hero V3[21] (an RGB camera for qualitative evaluation). Table 8 shows their respective camera intrinsics.

We have trained *DeepSfT* with a source RGB-D camera (Kinect V2), which has different intrinsics to the new cameras. We cannot immediately use images from the

Sequence Type	Samples	Registration (px)			3D Reconstruction (mm)						
		DOF	R50F	DeepSfT	CH17+GTR	CH17+DOF	CH17R+GTR	CH17R+DOF	HDM-net	R50F	DeepSfT
DB1S	3400	4.63	6.69	1.87	6.8968	15.60	8.27	15.41	10.80	7.99	1.68
DB2S	3400	5.91	6.13	1.34	6.89	28.26	8.27	28.04	9.92	7.75	1.63
DB1R	100	-	5.02	2.32	-	38.12	-	34.24	-	17.53	9.51
DB2R	230	-	4.13	1.53	-	27.31	-	25.24	-	14.45	7.3721

Table 4: Evaluation on synthetic and real databases *DB1S*, *DB2S*, *DB1R* and *DB2R*

Sequence Type	Samples	Registration (px)		3D Reconstruction (mm)			
		R50F	DeepSfT	CH17+GTR	CH17R+GTR	R50F	DeepSfT
DB3S	5000	7.14	1.05	-	-	6.34	1.16
DB4S	5000	8.93	3.60	73.80	70.70	12.62	1.57
DB3R	1300	-	-	-	-	12.43	5.12
DB4R	550	-	-	-	-	27.31	7.55

Table 5: Evaluation on synthetic and real databases *DB3S*, *DB4S*, *DB3R* and *DB4R*






















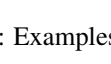
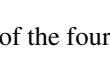

Input Image	Depth Output	Warp-U Output	Warp-V Output	Depth Error (mm)
				3.21
				4.69
				11.26
				8.96
				9.08
				7.49

Table 6: Examples of the four templates outputs

new camera because the network weights are specific to the intrinsics of the source camera. We propose to handle this by adapting the new camera’s effective intrinsics to match the source camera. Because the object’s depth within the training set varies (and so the perspective effects vary), we can emulate training with the new camera’s intrinsics simply by an affine transform of the new camera image. This eliminates the need to retrain the network. We assume lens distortion is either negligible or has been corrected *a priori* using *e.g.* *OpenCV*. The affine transform is given by $A = \text{diag}(f_u/f'_u, f_v/f'_v)$ and displacement $t = (c_u - c'_u f_u/f'_u, c_v - c'_v f_v/f'_v)^\top$, where f'_u, f'_v, c'_u, c'_v are the intrinsics of the new camera and f_u, f_v, c_u, c_v are the intrinsics of source camera di-


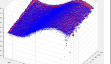

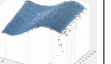


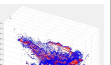


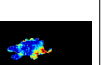

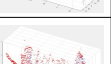



Input Image	Output vs GTH	Textured Output	Textured Groundtruth	Error Map
				
				
				

Table 7: Examples of 3D shapes recovered by *DeepSfT*

Cameras	Image Resolution	f_u	f_v	c_u	c_v
Kinect V2	1920x1080	1057.8	1064	947.64	530.38
Intel Realsense D435	1270x720	915.457	915.457	645.511	366.344
Gopro Hero V3	1920x1080	1686.8	1694.2	952.8	563.5

Table 8: Camera description table

vided by 4. The corrected image is then clipped about its optical centre and zero padded (if necessary), to obtain the resolution of 480×270 (the input image size of *DeepSfT*).

Table 9 gives 3D reconstruction error for Intel Realsense D435[26]. For the Gopro Hero V3[21] we show qualitative result.

Quantitatively the 3D reconstruction error of the original camera and the Intel Realsense D435[26] are quite similar. This clearly demonstrates the ability of *DeepSfT* to generalize well to images taken with a different camera. *DeepSfT* is able to cope with images from other cameras even if the focals are quite different as it is the case with the GoPro camera.

7.4 Light and Occlusion Resistance

We show that *DeepSfT* is resistant to light changes and significant occlusions. The first two rows of Table 10 show representative examples of scenes with external and








Camera	Converted Images	Results 	Depth error
Kinect V2			7.12
Realsense D435			12.34
Gopro Hero V3			–

Table 9: Results of experiments with different cameras (error in mm)

self occlusions for the thin-shell and volumetric objects. *DeepSfT* is able to cope with them, accurately detecting the occlusion boundaries. The third and fourth rows of




















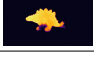










Occlusions					
Image					
Output					
Illumination Changes					
Input					
Output					
Failure Cases					
Input					
Points with information					

Table 10: Representative occlusion resistance, light resistance and failure cases.

Table 10 show examples of scenes with light changes that produce significant changes in shading. *DeepSfT* shows resistance to those changes.

7.5 Failure Modes

There are some instances where *DeepSfT* fails, shown in the final two rows of Table 10. There are general failure modes of SfT (very strong occlusions and illumination changes), for which all methods will fail at some point. We also have failure modes specific to a learning-based

approach (excessive deformations that are not represented in the training set).

7.6 Timing Experiments

Table 11 shows the average frame rates of the compared methods, benchmarked on a conventional Linux desktop PC with a single NVIDIA GTX-1080 GPU. The DNN-

	DeepSfT	R50F	CH17	CH17R	DOF
Time(fps)	20.4	37	0.75	0.193	8.84

Table 11: Frame rates of the evaluated methods.

based methods are considerably faster than the other methods, with frame rates close to real time (*DeepSfT*). Solutions based on *CH17* are far from real-time.

8 Conclusions

We have presented *DeepSfT*, the first dense, real-time solution for wide-baseline SfT with generic templates. This has been a long-standing computer vision problem for over a decade. *DeepSfT* will enable many real-world applications that require dense registration and 3D reconstruction of deformable objects, in particular augmented reality with deforming objects. We also expect it to be an important component for dense NRSfM in the wild. In the future we aim to improve results by incorporating temporal context information with recurrent neural networks, and to extend *DeepSfT* for unsupervised learning.

References

- [1] Agisoft Photoscan. <https://www.agisoft.com>. 6
- [2] A. Agudo and F. Moreno-Noguer. Simultaneous pose and non-rigid shape with particle dynamics. In *Proceedings of the IEEE Conference on Computer Vision and Pattern Recognition*, pages 2179–2187, 2015. 2
- [3] A. Agudo, F. Moreno-Noguer, B. Calvo, and J. M. M. Montiel. Sequential non-rigid structure from motion using physical priors. *IEEE Transactions on Pattern Analysis and Machine Intelligence*, 38(5):979–994, 2016. 2
- [4] V. Badrinarayanan, A. Kendall, and R. Cipolla. Segnet: A deep convolutional encoder-decoder architecture for image segmentation. *CoRR*, abs/1511.00561, 2015. 4

- [5] A. Bansal, B. Russell, and A. Gupta. Marr revisited: 2d-3d alignment via surface normal prediction. In *Proceedings of the IEEE conference on computer vision and pattern recognition*, pages 5965–5974, 2016. 2
- [6] A. Bartoli, Y. Gérard, F. Chadebecq, T. Collins, and D. Pizarro. Shape-from-template. *IEEE Transactions on Pattern Analysis and Machine Intelligence*, 37(10):2099–2118, 2015. 1, 2
- [7] Blender Online Community. *Blender - a 3D modelling and rendering package*. Blender Foundation, Blender Institute, Amsterdam. 6
- [8] C. Bregler, A. Hertzmann, and H. Biermann. Recovering non-rigid 3D shape from image streams. In *Proceedings of the Conference on Computer Vision and Pattern Recognition*. IEEE, 2000. 1
- [9] F. Brunet, A. Bartoli, and R. I. Hartley. Monocular template-based 3d surface reconstruction: Convex inextensible and nonconvex isometric methods. *Computer Vision and Image Understanding*, 125:138–154, 2014. 2
- [10] A. Chhatkuli, D. Pizarro, A. Bartoli, and T. Collins. A stable analytical framework for isometric shape-from-template by surface integration. *IEEE Transactions on Pattern Analysis and Machine Intelligence*, 39(5):833–850, 2017. 1, 2, 7
- [11] A. Chhatkuli, D. Pizarro, T. Collins, and A. Bartoli. Inextensible non-rigid structure-from-motion by second-order cone programming. *IEEE Transactions on Pattern Analysis and Machine Intelligence*, pages 1–1, 2017. 1
- [12] T. Collins and A. Bartoli. Using isometry to classify correct/incorrect 3D-2D correspondences. In *ECCV*, 2014. 3
- [13] T. Collins, A. Bartoli, N. Bourdel, and M. Canis. Robust, real-time, dense and deformable 3d organ tracking in laparoscopic videos. In *International Conference on Medical Image Computing and Computer-Assisted Intervention*, pages 404–412. Springer, 2016. 2, 3
- [14] T. Collins, P. Mesejo, and A. Bartoli. An analysis of errors in graph-based keypoint matching and proposed solutions. In *European Conference on Computer Vision*, pages 138–153. Springer, 2014. 2
- [15] J. B. Diederik P. Kingma. Adam: A method for stochastic optimization. *Arxiv*, arXiv:1412.6980(6), December 2014. 7
- [16] D. Eigen and R. Fergus. Predicting depth, surface normals and semantic labels with a common multi-scale convolutional architecture. In *Proceedings of the IEEE International Conference on Computer Vision*, pages 2650–2658, 2015. 2
- [17] D. Eigen, C. Puhrsch, and R. Fergus. Depth map prediction from a single image using a multi-scale deep network. In Z. Ghahramani, M. Welling, C. Cortes, N. D. Lawrence, and K. Q. Weinberger, editors, *Advances in Neural Information Processing Systems 27*, pages 2366–2374. Curran Associates, Inc., 2014. 4
- [18] R. Garg, V. K. BG, G. Carneiro, and I. Reid. Unsupervised cnn for single view depth estimation: Geometry to the rescue. In *European Conference on Computer Vision*, pages 740–756. Springer, 2016. 2
- [19] V. Gay-Bellile, A. Bartoli, and P. Sayd. Direct estimation of nonrigid registrations with image-based self-occlusion reasoning. *IEEE Transactions on Pattern Analysis and Machine Intelligence*, 32(1):87–104, Jan 2010. 2
- [20] V. Golyanik, S. Shimada, K. Varanasi, and D. Stricker. Hdm-net: Monocular non-rigid 3d reconstruction with learned deformation model. *CoRR*, abs/1803.10193, 2018. 2, 3, 7
- [21] GoPro. GoPro hero silver v3 rgb camera. <https://es.gopro.com/update/hero3>. 8, 9
- [22] R. A. Güler, N. Neverova, and I. Kokkinos. Densepose: Dense human pose estimation in the wild. *arXiv preprint arXiv:1802.00434*, 2018. 2
- [23] N. Haouchine and S. Cotin. Template-based monocular 3D recovery of elastic shapes using lagrangian multipliers. In *Proceedings of the IEEE Conference on Computer Vision and Pattern Recognition*. IEEE, July 2017. 2
- [24] N. Haouchine, J. Dequidt, M.-O. Berger, and S. Cotin. Single view augmentation of 3D elastic objects. In *ISMAR*, pages 229–236. IEEE, 2014. 2
- [25] R. Hartley and A. Zisserman. *Multiple view geometry in computer vision*. Cambridge university press, 2003. 1
- [26] Intel. Intel realsense d435 stereo depth camera. <http://realsense.intel.com>. 8, 9
- [27] L. Torresani, A. Hertzmann and C. Bregler. Nonrigid structure-from-motion: Estimating shape and motion with hierarchical priors. *IEEE Transactions on Pattern Analysis and Machine Intelligence*, 30(5):878–892, 2008. 1
- [28] F. Liu, C. Shen, G. Lin, and I. D. Reid. Learning depth from single monocular images using deep convolutional neural fields. *IEEE Transactions on Pattern Analysis and Machine Intelligence*, 38(10):2024–2039, 2016. 2
- [29] Q. Liu-Yin, R. Yu, L. Agapito, A. Fitzgibbon, and C. Russell. Better together: Joint reasoning for non-rigid 3d reconstruction with specularities and shading. *arXiv preprint arXiv:1708.01654*, 2017. 3
- [30] D. G. Lowe. Distinctive image features from scale-invariant keypoints. *International Journal of Computer Vision*, 60:91–110, 2004. 3
- [31] A. Malti, A. Bartoli, and R. Hartley. A linear least-squares solution to elastic shape-from-template. In *Proceedings*

- of the *IEEE Conference on Computer Vision and Pattern Recognition*, pages 1629–1637, 2015. 2
- [32] A. Malti, R. Hartley, A. Bartoli, and J.-H. Kim. Monocular template-based 3d reconstruction of extensible surfaces with local linear elasticity. In *Proceedings of the IEEE conference on computer vision and pattern recognition*, pages 1522–1529, 2013. 2
- [33] J. Martinez, R. Hossain, J. Romero, and J. J. Little. A simple yet effective baseline for 3d human pose estimation. In *Proceedings of the IEEE International Conference on Computer Vision*, volume 1, page 5, 2017. 2
- [34] P. K. Nathan Silberman, Derek Hoiem and R. Fergus. Indoor segmentation and support inference from rgb-d images. In *ECCV*, 2012. 6
- [35] D. T. Ngo, J. Östlund, and P. Fua. Template-based monocular 3d shape recovery using laplacian meshes. *IEEE Transactions on Pattern Analysis and Machine Intelligence*, 38(1):172–187, 2016. 1, 2, 3
- [36] E. Özgür and A. Bartoli. Particle-sft: A provably-convergent, fast shape-from-template algorithm. *International Journal of Computer Vision*, 123(2):184–205, 2017. 2
- [37] M. Perriollat, R. Hartley, and A. Bartoli. Monocular template-based reconstruction of inextensible surfaces. *International journal of computer vision*, 95(2):124–137, 2011. 2
- [38] J. Pilet, V. Lepetit, and P. Fua. Fast non-rigid surface detection, registration and realistic augmentation. *IJCV*, 76(2):109–122, February 2008. 3
- [39] D. Pizarro and A. Bartoli. Feature-based deformable surface detection with self-occlusion reasoning. *International Journal of Computer Vision*, 97(1):54–70, 2012. 2, 3
- [40] A. Pumarola, A. Agudo, L. Porzi, A. Sanfeliu, V. Lepetit, and F. Moreno-Noguer. Geometry-aware network for non-rigid shape prediction from a single view. In *Proceedings of the IEEE Conference on Computer Vision and Pattern Recognition*, pages 4681–4690, 2018. 2, 3
- [41] M. Salzmann and P. Fua. Reconstructing sharply folding surfaces: A convex formulation. In *Proceedings of IEEE Conference on Computer Vision and Pattern Recognition*, pages 1054–1061. IEEE, 2009. 2
- [42] M. Salzmann, F. Moreno-Noguer, V. Lepetit, and P. Fua. Closed-form solution to non-rigid 3d surface registration. *Computer Vision–ECCV 2008*, pages 581–594, 2008. 1, 2
- [43] K. H. X. Z. S. R. J. Sun. Deep residual learning for image recognition. *Arxiv*, arXiv:1512.03385, December 2015. 4, 7
- [44] S. N. B. T. and K. K. Dense point trajectories by gpu-accelerated large displacement optical flow. *ECCV*, 2010. 7
- [45] X. Wang, D. Fouhey, and A. Gupta. Designing deep networks for surface normal estimation. In *Proceedings of the IEEE Conference on Computer Vision and Pattern Recognition*, pages 539–547, 2015. 2
- [46] Y. B. Xavier Glorot, Antoine Bordes. Understanding the difficulty of training deep feedforward neural networks. *Proceedings MLR*. 7
- [47] Y. Dai, H. Li, and M. He. A simple prior-free method for non-rigid structure-from-motion factorization. In *Proceedings of the IEEE Conference on Computer Vision and Pattern Recognition*, 2012. 1